Adsorption
https://doi.org/10.1007/s10450-023-00417-8

Co–Fe–oxide nanoparticles supported on the various highly dispersed matrices: the effect of the carrier on structural and magnetic properties

Alla Dyachenko[1] · Konrad Terpilowski[2] · Olena Ischenko[3] · Iryna Sulym[1] · Dariusz Sternik[2] · Eugen Pakhlov[1,2] · Mykola Borysenko[1] · Lyudmila Storozhuk[4] · Lyudmila Andriyko[1] · Olena Goncharuk[5,6]

Received: 28 October 2022 / Revised: 4 July 2023 / Accepted: 22 September 2023

Abstracts

A series of mixed oxides was synthesized by deposition of the guest phase on the highly dispersed oxide matrix. Fumed nanooxides SiO_2, Al_2O_3, SiO_2/Al_2O_3, and $SiO_2/Al_2O_3/TiO_2$ with the specific surface area of 65–91 m^2/g were selected as highly dispersed matrices. Co–Fe mixed oxides with the general formula $Co_{4x}Fe_xO_y$ (Co: Fe = 4: 1) were deposited as the guest oxides using the two-step method: (i) solvate-stimulated modification of the surface of fumed nanocarriers with the mixture of cobalt nitrate (II) and iron (III) formate and (ii) subsequent heat treatment up to 600 °C to form $Co_{4x}Fe_xO_y$. The aim of this paper was to study the influence of the composition and structure of fumed oxide matrices and deposited guest phase on the morphology of the resulting composites in the gaseous and aqueous media using the XRD, XPS, FTIR, nitrogen adsorption and SEM/EDX, as well as quasi-elastic light scattering (QELS) methods. The low-temperature nitrogen adsorption isotherms have a sigmoidal shape with a narrow hysteresis loop characteristic of mesoporous materials. The specific surface area (S_{BET}) of the composites varies from 48 to 82 m^2/g, showing a tendency towards a decrease in the S_{BET} values by 10–26% in comparison with the initial nanocarriers. The SEM data show the denser aggregate structure of nanocomposites compared to the initial carriers. The primary particle size was in the 30–60 nm range and the EDX data confirm the formation of a guest phase on the mixed aluminosilicate carriers, mainly in the surface patches corresponding to the alumina structure. According to the QELS data, there is a tendency to form aggregates of 100–10 µm in size in the aqueous media. The XRD method shows that the deposited metal oxides are in the form of crystalline phases of Co_3O_4 with the crystallites of 25–26 nm in size for the individual SiO_2 and Al_2O_3 nanocarriers and 34–37 for the mixed ones, but the iron oxide reflections were not identified for the composites. XPS observation demonstrates the signal of Fe 2p electrons as the form of Fe_2O_3 oxide in the surface layer of nanocomposites as well as Co 2p as the Co_3O_4 and $Co(OH)_2$.

Keywords Oxide nanocomposites · Fumed mixed nanocarriers · $Co_{4x}Fe_xO_y$ · Structure formation · Particle size distribution · Superpara- and ferromagnetic properties

✉ Konrad Terpilowski
terpil@poczta.umcs.lublin.pl

[1] Chuiko Institute of Surface Chemistry, NASU, 17 General Naumov Str., Kiev 03164, Ukraine

[2] Maria Curie-Sklodowska University, M. Curie-Sklodowska Sq. 3, 20031 Lublin, Poland

[3] Taras Shevchenko National University of Kyiv, 64/13 Volodymyrs'ka Str., Kiev 01033, Ukraine

[4] UCL Healthcare Biomagnetics Laboratories, University College London, 21 Albemarle Street, London W1S 4BS, UK

[5] Ovcharenko Institute of Biocolloidal Chemistry, NAS of Ukraine, 42 Vernadskogo Blvd., Kiev 03142, Ukraine

[6] National Technical University of Ukraine «Igor Sikorsky Kyiv Polytechnic Institute», 37 Peremohy Av., Kiev 03056, Ukraine

Published online: 06 November 2023

1 Introduction

Nanotechnology is a topic which is currently being given a lot of attention by researchers because the unique chemical and physical properties of the nanomaterials have led to important roles in many scientific and industrial fields [1–3].

In particular, the current trend of the nanomaterials development is the synthesis of new sorbents with a large specific surface area and various active sites [4] for the effective interactions with various pollutant molecules, such as dyes [5–8], metal ions [9–13], high molecular weight compounds [14, 15]. High-dispersed oxides (SiO_2, Al_2O_3, TiO_2) can be used as effective agents in the processes of sorption [16] and flocculation [14, 17, 18] of water-soluble polymers. However, using highly dispersed sorbents in the form of fine powders in the liquid dispersion medium poses the task of their extraction after the sorption process. One of the ways to solve this problem is to create highly dispersed sorbents with additional functionality—magnetically sensitive composite nanomaterials [19, 20]. In most cases, the addition of nanomagnetite [21, 22] to the composition of such materials provides magnetic sensitivity but this has some limitations in the use, for example, high temperature can cause a decrease in magnetic properties [23]. In addition to magnetite, nickel and cobalt ferrites can exhibit magnetosensitivity. Immobilization of these compounds on the surface of highly dispersed oxides provides them with high thermal stability.

Furthermore, their interesting magnetic properties [24–26] suggest that they will have many applications in the magneto-optical recording media, displays and devices such as waveguides, insulators and switches [27]. There are different synthetic methods [28, 29] to prepare iron- and cobalt oxide nanoparticles: sol–gel [30], co-precipitation [31], plasma coating [32], sintering [33, 34], hydrothermal synthesis [35], and wetness- or incipient wetness impregnation [25]. Identifying the best combination of physical and chemical parameters for a specific application is a critical and ongoing research process [36]. The control over these parameters in metal oxide NPs for many applications is achieved by modifying the traditional synthetic procedures (following precipitation or high-temperature decomposition pathways) such as varying the temperature, the ratio of reactants, used surfactants, pH, or solvent [37, 38]. However, it remains a challenge to obtain ultrafine NPs with high stability and narrow size distribution. To overcome these limitations, a suitable and cost-effective strategy is grafting transition metal oxides on the surface of an appropriate material, in particular, highly dispersed supports. It has been reported that Co–Fe oxide nanoparticles were fabricated on various supports, including silica [27], alumina [39], zirconia [40] and Titania [25]. Among them, fumed silica dioxide (SiO_2) is highly mechanical and chemical stable, macroporous structure, has a large specific area, is environmentally friendly, and less toxic in nature [41–43]. For instance, the authors [44] obtained iron-cobalt nanoparticles dispersed in silica matrix and noted the formation of magnetic cobalt ferrite nanocomposites, Co_3O_4 and ferrihydrite or Co–Fe alloys, depending on the Fe and Co precursors. The previously synthesized nickel–cobalt oxide nanoparticles deposited on the fumed silica have proved themselves as promising catalysts for CO_2 methanation [45].

The synthesis of nanocomposites (NCs) based on the highly dispersed carriers with deposited metal oxides allows directing the design of a potential adsorbent towards increasing sorption properties and providing multifunctionality [46]. The introduction of Co–Fe nanoparticles into the structure of composites requires a study of the influence of synthesis conditions and the type of substrate on the structure and properties of NCs in general and the magnetosensitive phase in particular. The use of different carriers with different surface structures can affect significantly the structure of the deposited phase [47]. Moreover, there are no reports related to NCs based on the transition metals Co–Fe, supported on highly dispersed mixed nanooxides such as SiO_2/Al_2O_3 and SiO_2/Al_2O_3/TiO_2 with detailed investigations of their surface compositions. The presence of support provides new means to tailor the structural performance by altering the exposure of the active sites and modifying their nature through the interaction of the transition metal oxides with the support.

In the light of the above, the present paper was undertaken with the aim of analysing the influence of carries such as fumed silica, alumina, silica/alumina, and alumina/silica/titania on the formation of the grafted mixed oxide $Co_{4x}Fe_xO_y$ as well as the homogeneity, morphology and structure of the NCs as a whole.

2 Materials and methods

2.1 Materials

Fumed oxides SiO_2 (A-60), Al_2O_3, SiO_2/Al_2O_3 (SA96), and Al_2O_3/SiO_2/TiO_2 (AST1) (Pilot plant of Chuiko Institute of Surface Chemistry, Kalush, Ukraine) with similar values of the specific surface area (S_{BET}) of 65–91 m^2/g (Table 1) were used as nanocarriers. Fumed oxides are composed of spherical-like nonporous nanoparticles, whose diameter can be estimated as $d \approx 6/(\rho_0 S_{BET})$, where ρ_0 is the true density of nonporous nanoparticles. Cobalt nitrate hexahydrate ($Co(NO_3)_2 \cdot 6H_2O$, $\geq 98.5\%$, Merck) and iron (III) formate

Table 1 Composition of $Co_{4x}Fe_xO_y$/fumed oxide NCs

Sample	Composition of the fumed oxide carrier, % wt			m_{Me} in mixed $Co_{4x}Fe_xOy$/carrier, g per 1 g of fumed oxide		Co/Fe ratio (mmol per 1 g of fumed oxide carrier)	
	SiO_2	Al_2O_3	TiO_2	Co	Fe	Co	Fe
$Co_{4x}Fe_xO_y/SiO_2$	100	–	–	0.102	0.026	1.74	0.47
$Co_{4x}Fe_xO_y/Al_2O_3$	–	100	–	0.102	0.026	1.74	0.47
$Co_{4x}Fe_xO_y$/SA96	4	96	–	0.102	0.026	1.74	0.47
$Co_{4x}Fe_xO_y$/AST1	10	89	1	0.102	0.026	1.74	0.47

$(Fe(CHO_2)_3{\cdot}2H_2O$, 98%, Merck) were used as precursors to synthesize the nanooxides composites.

2.2 Synthesis of $Co_{4x}Fe_xO_y$—containing composites

$Co_{4x}Fe_xO_y$/nanocarrier composites (Table 1) were prepared using a two-stage method. The first stage was the solvate-stimulated modification of the surface of the initial fumed oxides with the mixture of Co(II) nitrate and Fe(III) formate in the ceramic ball-mill. The second stage consisted of drying and subsequent heating of the resulting mixture at 600 °C. The pre-modification of a fumed nanooxide carrier with the concentrated solutions of salts of the corresponding metals was performed in the 800 cm^3 ceramic ball-mill (ball size 2–3 cm, speed of 60 rpm) for 1.5 h. The mill was charged with 20 g of fumed oxide carrier and 10 ml of the aqueous solution of Co(II) nitrate (34.8 mmol) and Fe(III) formate (9.4 mmol) weighed to obtain a content in the deposits in the resulting composite. After achieving homogeneity, according to the microscopic examination, the resulting mixture was air-dried for 24 h. The dried powder was calcined at 600 °C for 1 h. The feature of the solvate-stimulated modification method is the homogeneous distribution of the solvated salt over the carrier surface. This is a required condition to form nanosized crystallites of the deposited oxide phase by the salt thermolysis upon the calcination at 600 °C.

2.3 Textural characterization

To analyse the textural characteristics of $Co_{4x}Fe_xO_y$/fumed oxide NCs, low-temperature (77.4 K) nitrogen adsorption–desorption isotherms were recorded using a Micromeritics ASAP 2405N adsorption analyzer. The samples were degassed at 110 °C for 2 h in the vacuum chamber. The values of the specific surface area (SSA, S_{BET}) were calculated according to the standard BET method [48]. The total pore volume V_p was evaluated by converting the volume of adsorbed nitrogen at $p/p_0 = 0.98$–0.99 (p and p_0 denote the equilibrium and saturation pressures of nitrogen at 77.4 K, respectively) to the volume of liquid nitrogen per gram of adsorbent. The nitrogen desorption data were used to compute the pore size distributions (PSD_S, differential f_V–dV_p/dR and f_S–dS/dR) using a self-consistent regularization (SCR) procedure under the non-negativity condition ($f_V \geq 0$ at any pore radius R) at a fixed regularization parameter $\alpha = 0.01$ with voids (V) between spherical nonporous nanoparticles packed in random aggregates (V/SCR model) [49]. The differential PSD_S with respect to the pore volume $f_V \sim dV/dR$, $\int f_V dR \sim V_p$ were re-calculated to incremental PSD (IPSD) at $\Phi_V(R_i) = (f_V(R_{i+1}) + f_V(R_i))(R_{i+1} - R_i)/2$ at $\sum \Phi_V(R_i) = V_p$. The f_V and f_S functions were also used to calculate contributions of nanopores (V_{nano} and S_{nano} at $0.35 < R < 1$ nm), mesopores (V_{meso} and S_{meso} at $1 < R < 25$ nm), and macropores (V_{macro} and S_{macro} at $25 < R < 100$ nm).

2.4 Scanning electron microscopy (SEM)

The surface morphology of composites was analyzed using the field emission Scanning Electron Microscopy employing a QuantaTM 3D FEG (FEI, USA) apparatus operating at the voltage of 30 kV.

2.5 X-ray powder diffraction

X-ray powder diffraction (XRD) patterns of metal oxide (as-synthesized) and metal NCs (after testing in the catalytic process) were recorded on the DRON-3 M diffractometer (Burevestnik, St.-Petersburg, Russia) with the monochromatic CuKα radiation (λ = 0.15418 nm) and the Ni filter over the angular range from 5° to 90°. The X-ray tube operation parameters were: voltage of 40 kV, current of 15 mA, scanning speed 2° min^{-1}. Interpretation of the phase composition was performed using the analytical software PDXL-2. The crystalline structure of the samples was analyzed using the JCPDS Database [50]. The average sizes of nanocrystallites (d, nm) were estimated according to the Scherrer equation [51] the calculations took into account the internal standard of the device (α-quartz)

$$d = \frac{K\lambda}{L\cos\theta} \quad (1)$$

where d is the dimension of the particle in the direction perpendicular to the reflecting plane, λ is the X-ray wavelength, K is the particle shape coefficient (equal to 0.9), L is the width of the reflex at half of its height, and θ is the scattering angle.

2.6 Fourier transform infrared (FTIR) spectroscopy

FTIR spectra of the powdered samples were recorded over the 4000–400 cm^{-1} range using the IR Spirit FTIR with the ATR mode.

2.7 X-ray photoelectron spectroscopy (XPS)

X-ray photoelectron spectroscopy (XPS) studies were performed using the multi-chamber UHV system (PREVAC). Spectra were collected using hemispherical Scienta R4000 electron analyser. Scienta SAX-100 x-ray source (Al Kα, 1486.6 eV, 0.8 eV band) equipped with the XM 650 X-Ray Monochromator (0.2 eV band) were used as a complementary equipment.

The pass energy of the analyser was set to 200 eV for survey spectra (with 750 meV step), and 50 eV for regions (high resolution spectra): C1s, O1s and N1s with 50 meV step). The base pressure in the analysis chamber was 5×10^{-9} mbar. During the spectra collection it was not higher than 3×10^{-8} mbar.

2.8 Particle size distribution in the aqueous media

Particle size distributions (PaSD) of NCs in the aqueous medium were studied with the Zetasizer Nano ZS (Malvern Instruments) apparatus using the universal dip cell (ZEN1002) (Malvern Instruments) and the wavelength $\lambda = 633$ nm and as well as the scattering angle of 13 and 176° at 298 K. The particle size determination accuracy and repeatability were ± 1–2%. The refractive index and absorption were 1.59 and 0.01, respectively. The samples for the PaSD measurement were prepared as follows: 0.1 wt% suspension of a composite in distilled water was sonicated for 3 min at 22 kHz using the ultrasonic disperser UZDN-A (500 W). The suspensions were equilibrated for 24 h and the PaSD were measured. The real information obtained from the experiment on the quasi-elastic light scattering is the distribution of light scattering intensity (PaDSI) from the objects by diffuse broadening. However, it is not the intensity distribution itself that is of interest but the associated particle size distribution related to the number ($PaDS_N$), or the molecular weight distribution ($PaDS_M$), or the related volume ($PaDS_V$). The collation of this information allows us to describe comprehensively the structure of NC suspensions. The transition from ($PaDS_I$) to these familiar characteristics of a polydisperse system requires the involvement of model ideas about the structure of the diffusers. To perform the measurements there was used, the computer program of the Malvern Instruments Company, which assumes that the particles are spherical.

2.9 Magnetic properties

Magnetic characterization of $Co_{4x}Fe_xO_y$/nanocarrier composites was made in the Quantum Design MPMS SQUID-VSM Evercool Magnetometer (San Diego, USA). The hysteresis loop (at 300 K and 5 K) was recorded with the applied magnetic fields between − 50 and 50 kOe. The saturation magnetisation for each sample was normalised by taking into account the metals content measured by the SEM/EDX analysis. The zero-field-cooled (ZFC) magnetization measurements were made after cooling the samples in the zero field to 5 K and measuring the magnetization while heating the samples up to 300 K in the magnetic field (H = 100 Oe). The field-cooled (FC) curve is measured by changing the temperature from 300 to 5 K.

3 Results and discussion

3.1 Textural characterization

The shape of the nitrogen adsorption–desorption isotherms (Fig. 1) can be attributed to type II with the hysteresis loop H3 of the IUPAC classification [48, 52] indicating the textural porosity of aggregates of nanoparticles. The presence of such a form of hysteresis loop indicates the dominant contribution of mesopores that are filled by nitrogen during the measurements.

The textural characteristics of oxide NCs calculated from the nitrogen adsorption isotherms are given in Table 2. The BET surface area and pore volume of composites (Table 2) depend on the specific surface area (SSA) values of the fumed oxide carriers. In general, after the modification of fumed oxides with Co–Fe mixed oxide, the SSA value of the composite decreases slightly for all carriers. The total pore volume and that of mesopores are typically greater for the composites than for the initial fumed oxides due to the compaction of the powders under the synthesis. The compaction results in a decrease in the empty volume ($V_{em} = 1/\rho_b - 1/\rho_0$, where ρ_b and ρ_0 denote the bulk and true densities of the powder materials) in the powders since the bulk density increases. However, the volume of mesopores can be increased due to the closer location of nonporous nanoparticles in their aggregates and agglomerates of aggregates [53]. All synthesized composites demonstrate pore size distributions with a predominant contribution from mesopores (Table 2, Fig. 2), which allows their classification as mesoporous materials.

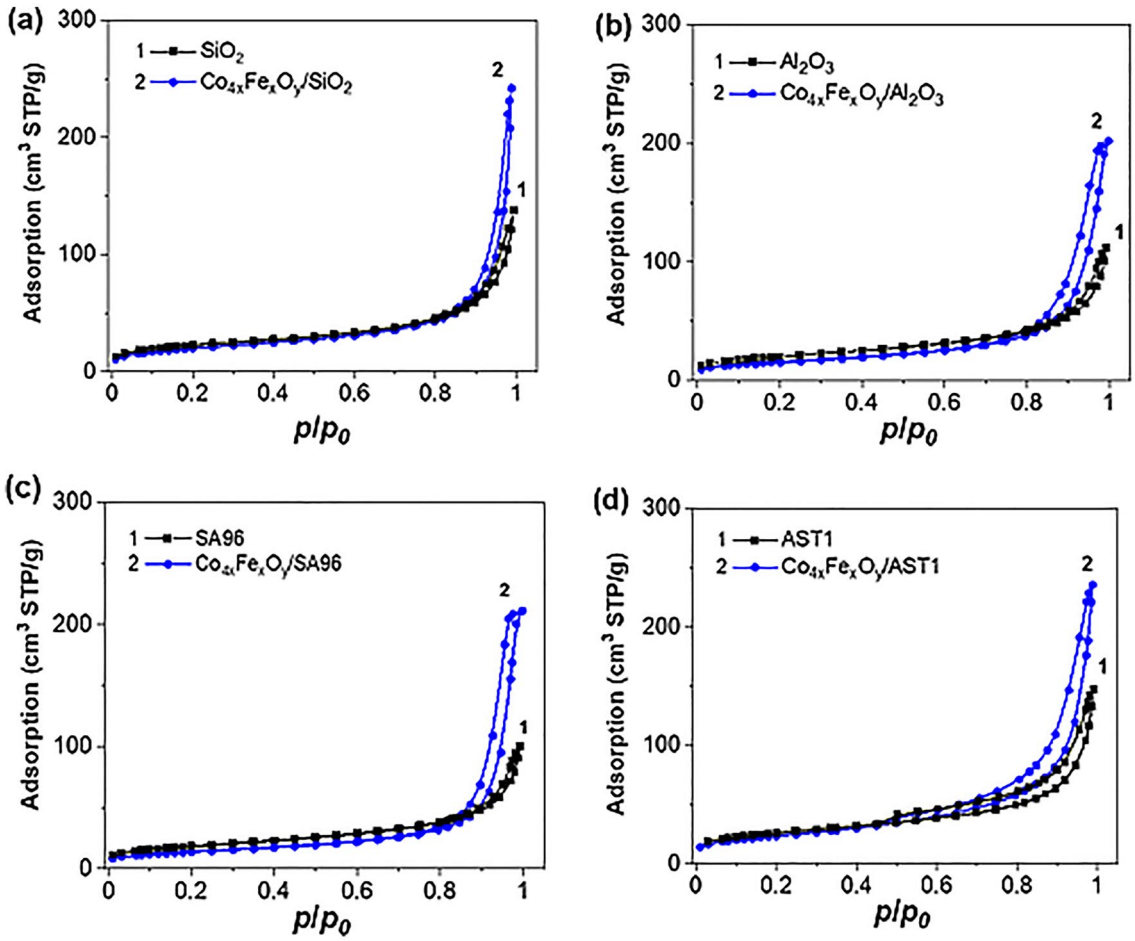

Fig. 1 Nitrogen adsorption–desorption isotherms for the initial fumed oxides and NCs: (a) SiO_2 and $Co_{4x}Fe_xO_y/SiO_2$, (b) Al_2O_3 and $Co_{4x}Fe_xO_y/Al_2O_3$, (c) SA96 and $Co_{4x}Fe_xO_y$/SA96 and (d) AST1 and $Co_{4x}Fe_xO_y$/AST1

Table 2 Textural characteristics of SiO_2, Al_2O_3, SA96, and AST1 supported Co–Fe oxides

Sample	S_{BET}, m^2/g	S_{micro}, m^2/g	S_{meso}, m^2/g	S_{macro}, m^2/g	V_{micro}, cm^3/g	V_{meso}, cm^3/g	V_{macro}, cm^3/g	V_p, cm^3/g	$R_{p,V}$ nm
SiO_2	80	32	45	3	0.014	0.13	0.07	0.21	23.9
$Co_{4x}Fe_xO_y/SiO_2$	71	21	40	10	0.010	0.16	0.20	0.37	31.2
Al_2O_3	72	21	50	1	0.010	0.11	0.05	0.17	20.6
$Co_{4x}Fe_xO_y/Al_2O_3$	56	12	43	2	0.006	0.27	0.04	0.31	16.0
SA96	65	21	42	3	0.009	0.10	0.05	0.15	21.7
$Co_{4x}Fe_xO_y$/SA96	48	15	31	2	0.008	0.28	0.04	0.33	17.2
AST1	91	26	62	4	0.010	0.14	0.08	0.27	22.5
$Co_{4x}Fe_xO_y$/AST1	82	14	63	5	0.006	0.27	0.09	0.36	19.5

Specific surface area in total (S_{BET}), of nanopores (S_{nano}), mesopores (S_{meso}), macropores (S_{macro}) and pore volumes (V_p, V_{nano}, V_{meso}, V_{macro}) at the pore radius $R < 1$ nm, 1 nm $< R <$ 25 nm, and $R >$ 25 nm, respectively. $R_{p,V}$ represents the average pore radius

The pore size distribution functions (Fig. 2) confirm the conclusion based on the isotherm shapes (Fig. 1) that the composites are mainly mesoporous since the contributions of micropores and macropores are small (Table 2). The first peak is due to the really small contribution of nanopores at R < 1 nm. However, the second one is due to the ineffective adsorption of nitrogen in the macropores because the interactions of nitrogen molecules with large distant nanoparticles are very weak. Therefore, nitrogen molecules in the bound fluid are not predominant in broad macropores. The first peak of the PSD (Fig. 2) corresponds to the narrow voids between the nanoparticles

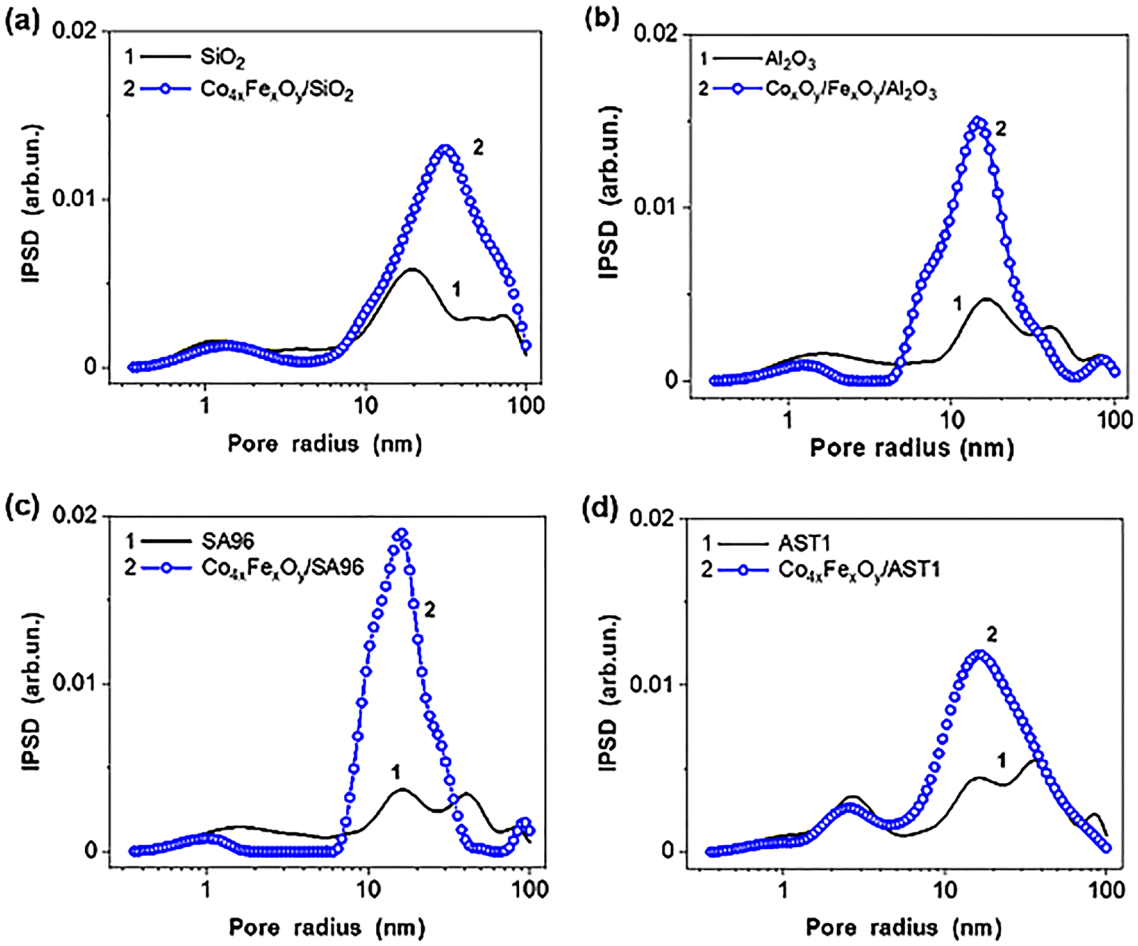

Fig. 2 Incremental pore size distributions for initial fumed oxides and NCs: (a) SiO_2 and $Co_{4x}Fe_xO_y/SiO_2$, (b) Al_2O_3 and $Co_{4x}Fe_xO_y/Al_2O_3$, (c) SA96 and $Co_{4x}Fe_xO_y$/SA96 and (d) AST1 and $Co_{4x}Fe_xO_y$/AST1

closely located in the same aggregates. Broader voids can be present between the distant nanoparticles in the same aggregate or neighbouring aggregates.

The contribution of macropores increases significantly (Fig. 2) for all samples $Co_{4x}Fe_xO_y$/nanocarrier, except for $Co_{4x}Fe_xO_y/SiO_2$, for which it remains almost unchanged. The total pore volume V_p and the volume of mesopores increase for all composites compared to the initial fumed oxides (Table 2). As a result, the changes in the pore volume depend on the type of support, features of the second phase formation, decrease in the void volume in the aggregates of nanoparticles, and the difference in the true density of the deposited oxide particles and fumed oxide carriers that is minimal for silica.

3.2 Scanning electron microscopy

The SEM images of $Co_{4x}Fe_xO_y$/fumed oxide NCs (Figs. 3 and 4) show the formation of $Co_{4x}Fe_xO_y$ particles at the nanocarrier surface. As shown in Figs. 3 and 4, it can be observed that the $Co_{4x}Fe_xO_y$ nanoparticles (NPs) appear in the uniform sphere-like shape and homogeneous distribution. The aggregated structures of grafted oxides of 20 to 40 nm in size were well observed for $Co_{4x}Fe_xO_y/SiO_2$, $Co_{4x}Fe_xO_y/Al_2O_3$ (Fig. 3b, d), $Co_{4x}Fe_xO_y$/SA96 (Fig. 4b) and 80–120 nm for $Co_{4x}Fe_xO_y$/AST1 (Fig. 4d). As a whole, the composites look more compact than the initial fumed nanocarriers.

According to the SEM/EDX data (Table 3), it can be seen that in the case of mixed fumed oxides as carriers, the surface content of aluminium is significantly reduced. This indicates that the synthesis of the deposited oxide phase occurs mainly in the areas corresponding to the Al_2O_3 patches: for the Al_2O_3-based composite the decrease in the Al surface concentration was from 50.8 to 34.5%, for the SA96-based composite it was from 48.1 up to 33.6%, for the AST1-based composite it was from 41.8 up to 27.4%.

The surface concentration of Ti atoms also decreases for the AST1-based NCs more than doubled, indicating that the patches of the surface having TiO_2 or the solid solution

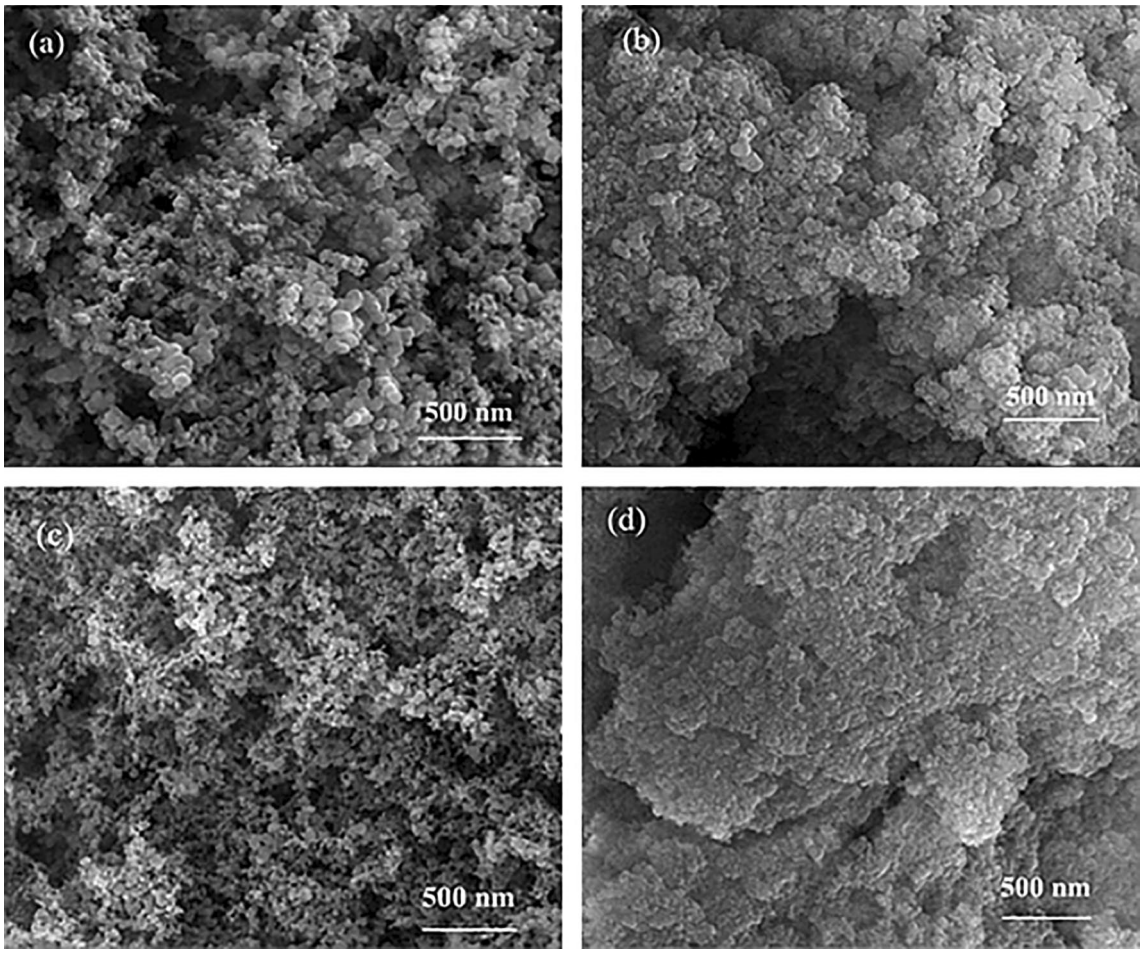

Fig. 3 SEM images of the initial nanocarriers SiO_2 (**a**), Al_2O_3 (**c**), and $Co_{4x}Fe_xO_y/SiO_2$ (**b**), $Co_{4x}Fe_xO_y/Al_2O_3$ (**d**) NCs

structure with the bridge-type Ti–O–Si or Al–O–Ti sites also take part in the interactions with the deposited phase. At the same time, the Si concentration increases in the composites based on the mixed SA96 and AST1 nanocarriers which indicate that the regions with a structure corresponding to SiO_2 remain not involved in the interactions with the deposited phase. The Co and Fe surface concentrations depend insignificantly on the carrier nature and it varies for Co from 14.9 to 15.0 over the individual carriers (Al_2O_3 and SiO_2) and 14.4–14.5 over the mixed carriers (SA96 and AST1) and 3.4–4.1 for Fe. The average Co/Fe wt% ratio calculated from the SEM/EDX data for all NCs is very close to the given values upon the component ratio in the synthesis (Co: Fe = 4: 1).

3.3 X-ray powder diffraction analysis

The XRD patterns of $Co_{4x}Fe_xO_y$/fumed oxide NCs (Fig. 5) showed only a cubic cobalt oxide Co_3O_4 phase formed on the surface of carriers. The diffraction peaks at $2\theta = 19.0$; 31.2; 36.8; 44.63; 58.98; 65.1 correspond to the reflections (111), (202), (311), (400), (511), (404) of Co_3O_4. The size of the cobalt oxide crystallites calculated from the plane (311) according to the Scherrer equation is 25–37 nm (Table 4). Smaller crystals are formed on the surface of individual oxides, and the surface of mixed oxides promotes the formation of larger particles. The iron, which was introduced into the composition of NCs by the method of solvate-stimulated surface modification of highly dispersed oxides, is not identified, as an individual phase by the XRD method. The registration of iron compound is complicated due to its low content in the NCs composition and can be under the XRD device sensitivity.

3.4 IR spectroscopy

The IR spectra of the synthesized $Co_{4x}Fe_xO_y$/fumed oxide NCs were characterized using the FTIR spectroscopy in the wavenumber range 4000–400 cm^{-1} and are shown in Fig. 5. Comparing the IR spectra of initial fumed oxides used for the synthesis with the spectra of synthesized $Co_{4x}Fe_xO_y$/fumed oxide NCs (Fig. 6), it should be noted that in all

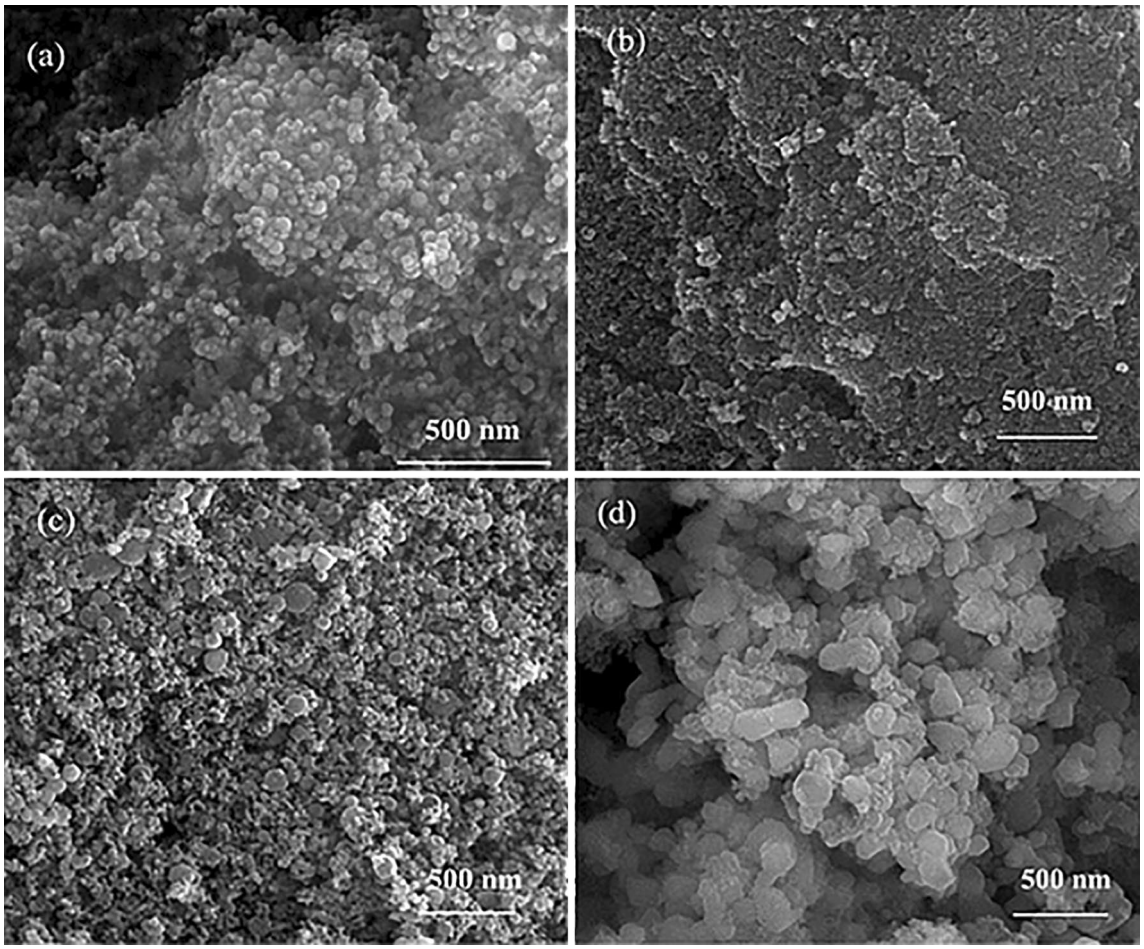

Fig. 4 SEM images of initial nanocarriers SA96 (**a**), AST1 (**c**) and $Co_{4x}Fe_xO_y$/SA96 (**b**) and $Co_{4x}Fe_xO_y$/AST1 (**d**) NCs

Table 3 SEM/EDX data

Sample	Si wt%	Al wt%	Ti wt%	O wt%	Co wt%	Fe wt%
SiO_2	36.9	–	–	63.1	–	–
$Co_{4x}Fe_xO_y/SiO_2$	31.4	–	–	50.0	14.9	4.1
Al_2O_3	–	50.8	–	49.2	–	–
$Co_{4x}Fe_xO_y/Al_2O_3$	–	34.5	–	47.0	15.0	3.4
SA96	0.06	48.1	–	51.9	–	–
$Co_{4x}Fe_xO_y$/SA96	1.5	33.6	–	47.1	14.5	3.3
AST1	5.3	41.8	1.3	51.6	–	–
$Co_{4x}Fe_xO_y$/AST1	7.4	27.4	0.6	46.9	14.4	3.4

spectra characteristic bands are observed in the ranges: the broadband between 3700 and 3100 cm^{-1} refers to the stretching vibrations of OH groups sourced from various forms of adsorbed water. The band at 1636 cm^{-1} corresponds to the deformation vibrations of water molecules. The broad intensive stretching vibrations of Si–O–Si at 1100 cm^{-1} (asymmetric) and 800 cm^{-1} (symmetric) are observed in the silica-based composites.

To characterize the deposited $Co_{4x}Fe_xO_y$ phase, the initial IR spectra were processed mathematically: the spectrum of the initial nanocarrier was subtracted from the spectrum of the $Co_{4x}Fe_xO_y$/fumed oxide NCs and the remaining spectrum was decomposed using the Origin7.5 PeakFit, which made it possible to estimate the presence and characteristic frequency of peaks assigned to the Co–O and Fe–O bonds in different sites (Table 5).

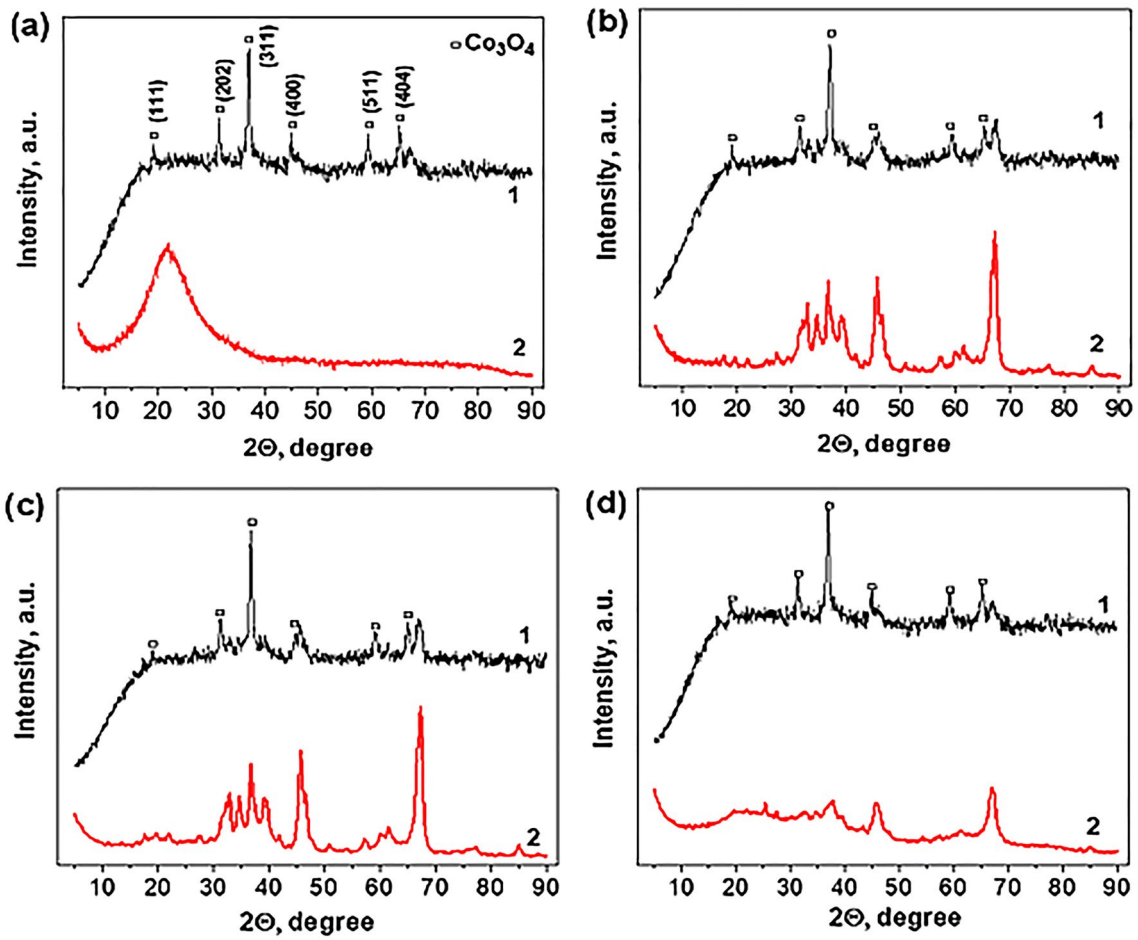

Fig. 5 XRD spectra of $Co_{4x}Fe_xO_y$ oxides particles formed on the surface of (**a**) SiO_2, (**b**) Al_2O_3, (c) SA96 and (**d**) AST1, where curve 1—the pattern of the NC and curve 2—the pattern of the appropriate carrier

Table 4 The size of crystallites formed on the NCs surface

Sample	Crystallites	2θ, deg	*D*, nm
$Co_{4x}Fe_xO_y/SiO_2$	Co_3O_4	36.8	25
$Co_{4x}Fe_xO_y/Al_2O_3$	Co_3O_4	36.8	26
$Co_{4x}Fe_xO_y$/SA96	Co_3O_4	36.8	37
$Co_{4x}Fe_xO_y$/AST1	Co_3O_4	36.8	34

The bands in the region of 300–700 cm^{-1} are assigned to the fundamental vibrations of the metal (M) ions of the crystal lattice in the octahedral and tetrahedral positions [54]. The peak at 652–664 cm^{-1} corresponds to the intrinsic stretching vibrations of the cobalt in the tetrahedral site, Co^{2+}–O [55] in the tetrahedral position, and 551–567 cm^{-1} are assigned to Co^{3+}–O in the octahedral position. The absorption band at 525–623 cm^{-1} can be attributed to the stretching vibrations of Fe–O in the tetrahedral and octahedral sites. Based on the literature data [56, 57] the high-frequency bands about (600–700 cm^{-1}) are attributed to the tetrahedral group, and the low-frequency band (about 350–450 cm^{-1}) is attributed to the octahedral group, Fe in the obtained composites is more likely to belong to the tetrahedral sites while the formation of the structure of the solid solution.

3.5 X-ray photoelectron spectroscopy

The surface analysis of Co–Fe oxides NCs was performed using the XPS method. The survey spectra indicate the presence of O, Fe and Co at the surface of all NCs as well as Al and/or Si at the surface of NCs based on the appropriate carrier. Figures 7 and 8 show typical core-level spectra of Co $2p_{3/2}$ and Fe $2p_{3/2}$ for synthesized NCs respectively. Experimental E_b values of Co $2p_{3/2}$ and Fe $2p_{3/2}$ core-level XPS spectra of investigated Co–Fe nanocomposites are presented in Table 6. The XPS peak areas were used for the calculation of Co/Fe and $Co_3O_4/Co(OH)_2$ ratios.

Fitting of Co $2p_{3/2}$ XPS spectra was provided according to the model proposed by Biesinger [58]. XPS signal of Co 2p electrons can be convoluted into two groups of multiple

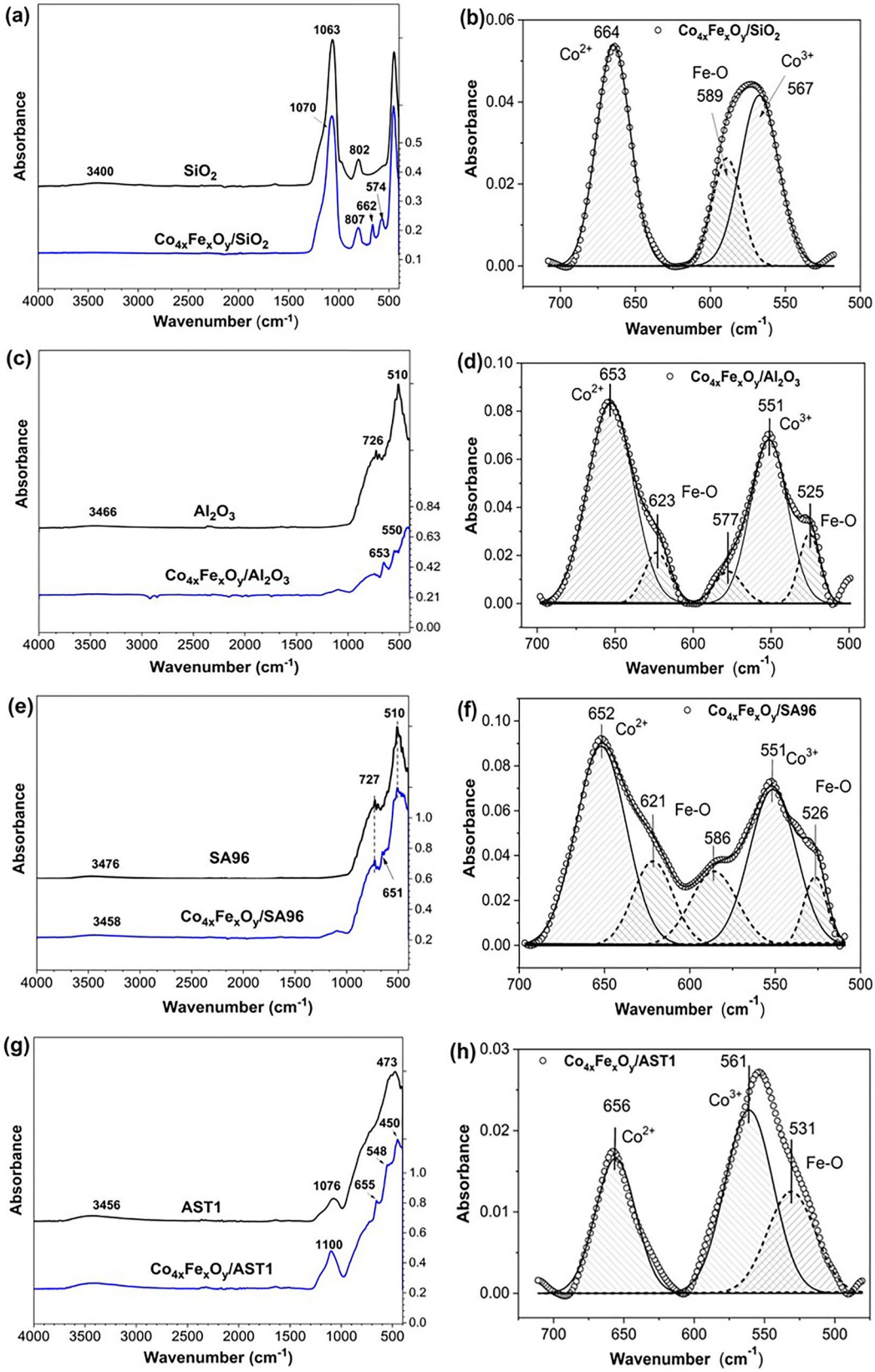

Fig. 6 IR spectra of $Co_{4x}Fe_xO_y$/fumed oxides NCs: (a, b) SiO_2 and $Co_{4x}Fe_xO_y/SiO_2$, (c, d) Al_2O_3 and $Co_{4x}Fe_xO_y/Al_2O_3$, (e, f) SA96 and $Co_{4x}Fe_xO_y$/SA96 and (g, h) AST1 and $Co_{4x}Fe_xO_y$/AST1

Table 5 The characteristic bands assigned to the M–O bonds in the FTIR spectra of NCs

Sample	ν, cm^{-1}		
	Co^{2+}–O	Co^{3+}–O	Fe–O
$Co_{4x}Fe_xO_y/SiO_2$	664	567	589
$Co_{4x}Fe_xO_y/Al_2O_3$	653	551	623, 577, 525
$Co_{4x}Fe_xO_y/SA96$	652	551	621, 586, 526
$Co_{4x}Fe_xO_y/AST1$	656	561	531

peaks for all of the investigated NCs. The multiple peaks depicted as 1–4 (Fig. 7a–d) with the binding energy of $2p_{3/2}$ electrons within the range of 776.7–789.6 eV and multiplet of A–D in the range of 780.5–790.5 eV corresponded to Co_3O_4 and $Co(OH)_2$ species respectively. The calculated data of atomic % concentrations of corresponding types specified the high level of $Co(OH)_2$ on the surface of NCs. There are two possible reasons for the $Co(OH)_2$ signal on the surface of NCs. The first suggestion is not entirely decomposition of $Co(NO_3)_2{\cdot}6H_2O$ modifying salts with formation of stable half-product means $Co(OH)_2$ and other one is the secondary hydroxylation of Co^{2+} surface particles. We declare that the synthesis conditions ensure the entire destruction of grafted modifying nitrate groups with the resulting formation of Co_3O_4. This is confirmed with XRD results showed the presence Co_3O_4 compounds in the structure on synthesized NCs. Therefore, the presence of cobalt hydroxide on the surface of NCs can occur as a result of hydroxylation of the surface of NCs. The important observation is concerning of $Co_3O_4/Co(OH)_2$ ratio for the different NCs. It is noted that the calculated amount of Co_3O_4 in the surface layer of SiO_2 based NC is higher than for other carriers. It seems that amorphous SiO_2 is more appropriate for Co_3O_4 formation in the surface layer of NCs than crystallinity carrier based on the Al_2O_3 (Al_2O_3, SA96, AST1). The calculated Co/Fe ratio in the surface layer of Co–Fe NCs (see Table 6) does not correspond to specified in the synthesis routine as Co:Fe = 4:1. It follows that approximately 25% of grafted cobalt compounds are presented on the surface layer and significant part of cobalt can be localized in the pores of NCs. XPS research results show the presence of Fe(III) in the surface layer of

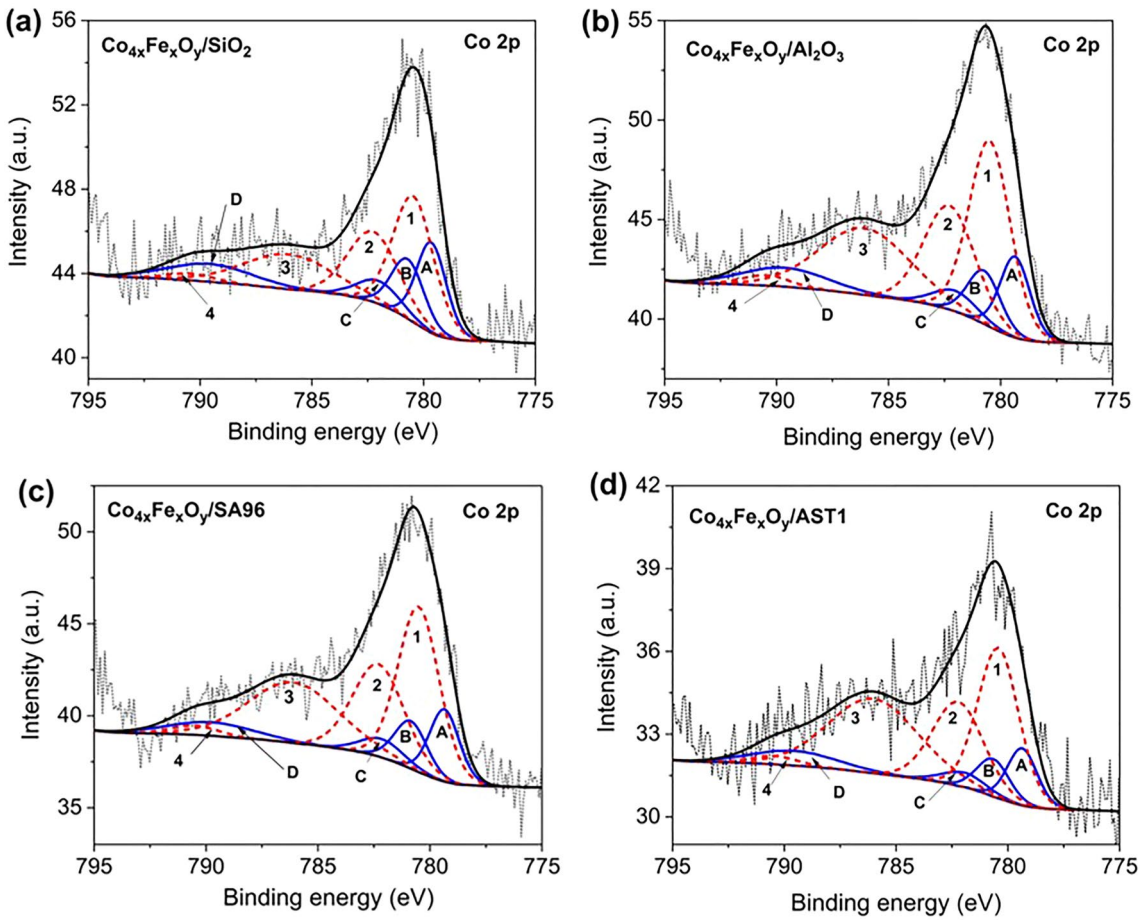

Fig. 7 Co $2p_{3/2}$ XPS spectra of NCs based on SiO_2 (**a**), Al_2O_3 (**b**), SA96 (**c**) and AST1 (**d**). The peaks 1–4 are affiliated with Co_3O_4 and peaks A–D with $Co(OH)_2$

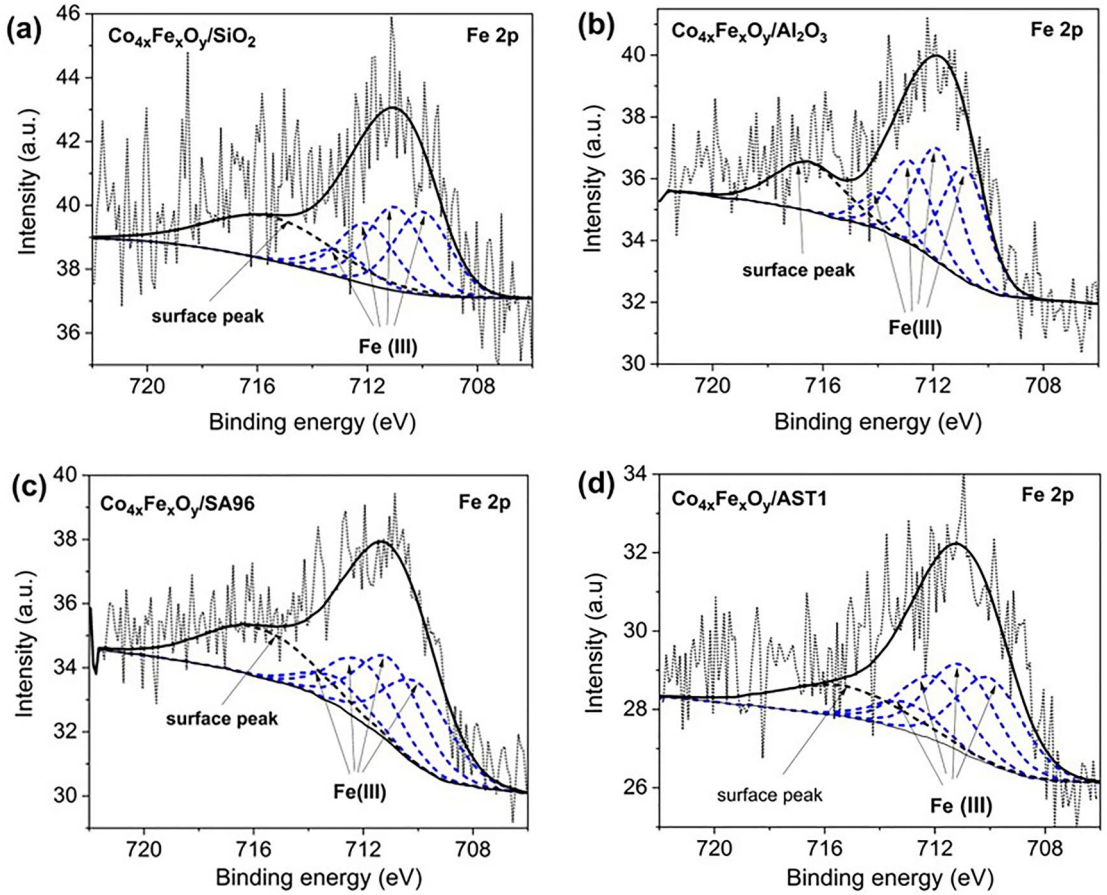

Fig. 8 Fe $2p_{3/2}$ XPS spectra of NCs based on SiO_2 (**a**), Al_2O_3 (**b**), SA96 (**c**) and AST1 (**d**)

Table 6 Experimental E_b values obtained from Co $2p_{3/2}$ and Fe $2p_{3/2}$ XPS spectra of Co–Fe nanocomposites

Sample	E_b, eV			Atomic ratio, %	
	Fe(III)	Co(II) + Co(III)	Co(II)		
	Fe_2O_3	Co_3O_4	$Co(OH)_2$	$Co_3O_4/Co(OH)_2$	Co/Fe
Co–Fe/SiO_2	710.0–713.0	779.6–789.6	780.5–790.5	3.1/96.9	56/44
Co–Fe/Al_2O_3	710.8–713.8	779.4–789.6	780.5–790.5	1.8/98.2	61/39
Co–Fe/SA96	710.0–713.0	779.4–789.8	780.5–790.5	1.7/98.3	47/53
Co–Fe/AST1	710.0–713.0	779.4–789.6	780.4–790.4	1.7/98.3	46/54

nanocomposites [58–60]. The most possible compound of Fe (III) that can be formed on the surface of NCs is Fe_2O_3 [60]. Moreover, the chemical transformation of iron containing surface modification agent (iron formate) leads to the formation of Fe_2O_3 under the presented synthesis condition. The formation of Fe_3O_4 is doubtful because it requires either significantly higher temperatures or a reducing atmosphere.

The XPS signal of O 1 s electrons was de-convoluted into several peaks (Fig. 8) related to the carrier matrix and CoFe modified oxides. Experimental E_b values obtained from O 1 s XPS spectra and atomic % calculated as the integrated square of the de-convoluted peaks are provided in Table 7. The main components of oxygen bonds have been identified and related to the highly dispersed matrices of NCs. XPS signals of O 1 s electrons with E_b at 532.7

Table 7 Experimental E_b values obtained from O $1s_{1/2}$ XPS spectra of Co–Fe nanocomposites

Sample	Species	E_b, eV	At%
Co–Fe/SiO_2	Si–O	532.7	74.4
	Si–OH	533.3	18.9
	O^{-2}	530.2	4.1
	HO–	531.3	1.9
	H_2O	535.5	0.76
Co–Fe/Al_2O_3	Al–O	531.7	46.6
	Al–OH	532.9	21.7
	O^{-2}	529.8	3.0
	HO–	530.7	28.1
	H_2O	535.1	0.6
Co–Fe/SA96	Al–O	531.7	46.5
	Al–OH	532.8	15.4
	O^{-2}	529.7	4.8
	HO–	530.6	33.1
	H_2O	534.9	0.18
Co–Fe/AST1	Al–O	531.7	33.8
	Al–OH	532.9	17.7
	Si–O	532.7	17.3
	Si–OH	533.4	8.8
	O^{-2}	529.8	2.4
	HO–	530.7	16.8
	H_2O	534.3	3.2

and 533.3 ± 0.1 eV can be associated with Si–O and Si–OH moieties presented on the surface of SiO_2 and AST1-based NCs. For the NCs based on Al_2O_3, SA96 and AST1 appropriate O 1 s signals with E_b at 531.7 and 532.8 ± 0.1 eV related with Al–O and Al–OH moieties [61]. The presence of physisorbed water was identified as a peak of very low intensity located at the region of higher binding energies around 534 eV (Table 7). The XPS signals of O 1 s electrons corresponded to O^{2-} and –OH moieties are positioned at ~ 529.8 and ~ 530.7 eV respectively for the Co–Fe/Al_2O_3, Co–Fe/SA96 and Co–Fe/AST1 NCs and shifted to the 530.2 and 531.3 eV for Co–Fe/SiO_2. These experimental XPS observations suggest that O^{2-} particles can be attributed to fragments of metal oxides (Co and Fe) deposited on the surface of the carrier, and HO– particles are associated with $Co(OH)_2$ groups found on the surface of NCs (Fig. 9).

3.6 Particle size distribution in the aqueous medium

The quasi-elastic light scattering (QELS) method allows determining the particle size distribution (PaSD) in the aqueous medium. The results of measurements for the synthesized samples of mixed oxides are presented in the form of the dependence of the particle size distribution for their number $PaSD_N$ (Fig. 10a, c) and volume $PaSD_V$ (Fig. 10b, d). The modification of silica with Co and Fe oxides leads to an increase in the particle sizes due to the formation of the second oxide phase and enhanced aggregation during the synthesis. The degree of aggregation/agglomeration depends on the characteristics of nanoparticles and their interactions in the dispersion media. The initial fumed oxides (SiO_2, Al_2O_3, SA96) are characterized by nearly monomodal PaSD related to the particle numbers with the maximum at 100–110 nm (Fig. 10), except for AST1 having more complicated particulate morphology.

The $PaSD_N$ of the composites are mono- or bimodal (Fig. 10a, c) and three peaks are observed for $PaSD_V$ (Fig. 10b, d): aggregates ~ 90 and ~ 430 nm (SiO_2) and large agglomerates > 5.5 μm are presented in the aqueous dispersion of composites after the ultrasonic treatment. It should be noted that although for the composites $PaSD_N$ shows the maximum at 85–103 nm for SiO_2 and the SA96 carrier, i.e., the number of small secondary particles of ~ 100 nm is larger than the number that of large aggregates (> 1 μm). However, according to $PaSD_V$, the volume of aggregates > 1 μm for these composites is much higher than that for the initial nanocarriers. The PaSD for the Co- and Fe-containing composites supported on Al_2O_3 and AST1 is characterized by the presence of aggregates and agglomerates of larger sizes (~ 1.1–1.3 and 5.5 μm). The aggregates smaller than 1 μm in size are not observed in the dispersion. This indicates stronger bonds of the deposited guest oxide with the support.

3.7 Magnetic properties

The magnetic properties of $Co_{4x}Fe_xO_y$/fumed oxide NCs and their magnetization curves are shown in Table 8 and Fig. 11 of the samples. The hysteresis loop with the superparamagnetic behaviour for $Co_{4x}Fe_xO_y$/SA96 and $Co_{4x}Fe_xO_y/A_2O_3$ (H_c = 43.05 Oe and 56.5 Oe respectively) and the mix of superpara- and ferromagnetic for the $Co_{4x}Fe_xO_y$/Si60 and $Co_{4x}Fe_xO_y$/AST1 nanocomposites (H_c = 386.5 Oe, and 117.8 Oe, respectively) are pointed out to. The influence of the nonmagnetic phase (nanocarriers) was manifested in the relatively small total magnetization of the synthesized NCs. Apparently, the magnetic properties of the samples $Co_{4x}Fe_xO_y/SiO_2$, $Co_{4x}Fe_xO_y/Al_2O_3$, $Co_{4x}Fe_xO_y$/SA96 and $Co_{4x}Fe_xO_y$/AST1 are influenced by the fraction of pores and their distribution in the composites. Porosity leads to decreased density, impeding magnetic domain rotation in the direction of the magnetic field thus reducing the ability of magnetic conductivity [62, 63]. Pores act as air gaps in the magnetic circuit and decrease the permeability of the material.

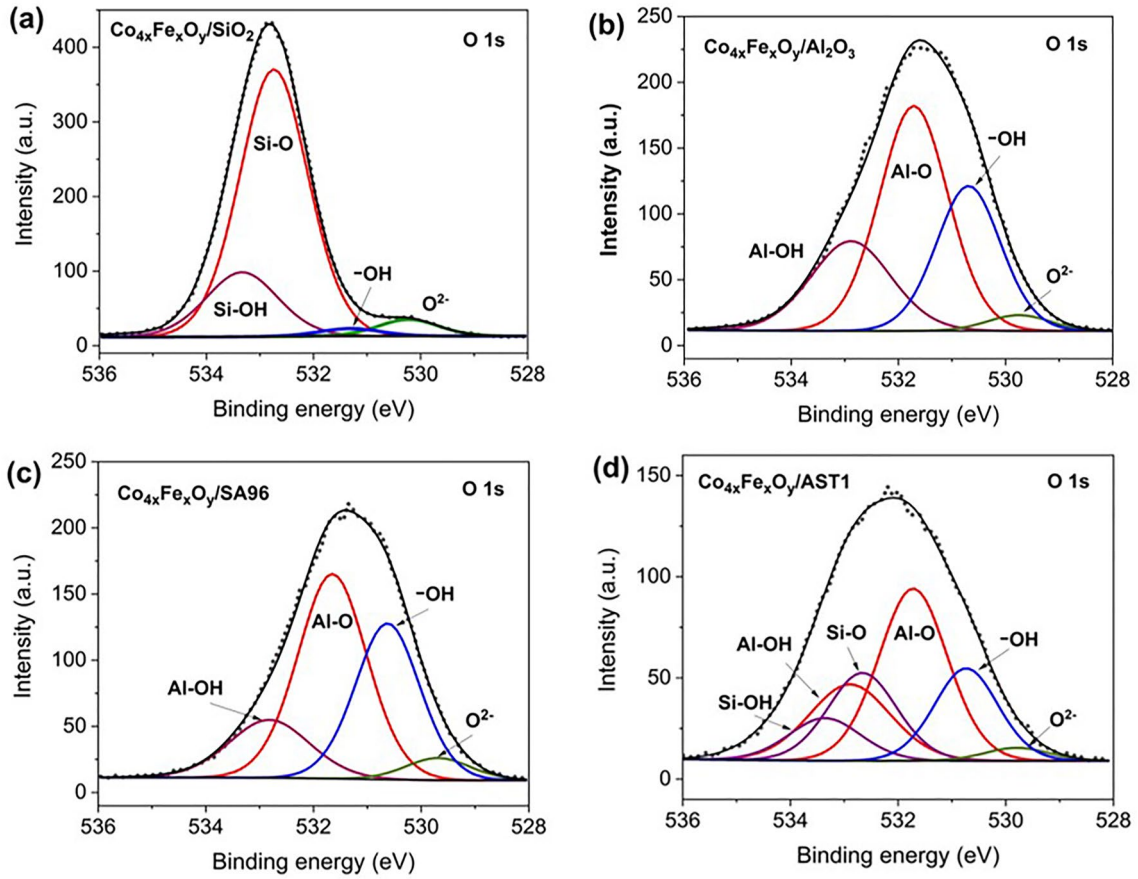

Fig. 9 O $1s_{1/2}$ XPS spectra of NCs based on SiO_2 (**a**), Al_2O_3 (**b**), SA96 (**c**) and AST1 (**d**)

The ZFC and FC (Fig. 12) curves at 100 Oe reveal that the blocking temperature for the $Co_{4x}Fe_xO_y$/fumed oxide NCs with the crystallite size around 25–37 nm (Table 8) is much above room temperature (300 K) for all NCs. The studied samples show a mixture of superpara- and ferromagnetic behaviour below the blocking temperature i.e., 300 K. The relatively larger blocking temperature might be due to the large anisotropy in $Co_{4x}Fe_xO_y$ phase.

4 Conclusions

The series of novel $Co_{4x}Fe_xO_y$/fumed oxide nanocomposites were synthesized by the thermooxidation of metal salts adsorbed onto the individual and complex fumed nanooxides. The effects of the support structure were analyzed with respect to the formation of the deposited phases. The phase composition and average sizes of crystallites determined from the XRD data show that the Co_3O_4 phase in the $Co_{4x}Fe_xO_y$/fumed oxide nanocomposites includes crystallites of 25–37 nm in diameter while the iron oxide reflections are not practically identified. The results of XPS measurements are in the good agreement with the FTIR spectroscopy: these methods demonstrated the presence of Co (II) and Co (III) compounds on the surface of nanocomposites as well as XRD result demonstrated formation the crystallites of Co_3O_4 that can be formed in the porous structure of nanocomposites. According to the SEM/EDX data, the formation of the deposited $Co_{4x}Fe_xO_y$ phase occurs mainly on the nanocarrier surface corresponding to the Al_2O_3 structure patches or solid solution structures with the bridge bonds Al–O–Ti, Al–O–Si and Si–O–Ti. The specific surface area of the composites decreases insignificantly when the phase $Co_{4x}Fe_xO_y$ is deposited on the support. The incremental pore size distribution functions show predominantly the mesoporosity of nanocomposites, the volume of mesopores increases significantly in comparison to the initial fumed oxides. According to the QELS data for the aqueous dispersions of the synthesized nanocomposites, small aggregates with several nanoparticles of 100 nm in size, large aggregates up to ~ 1 μm, and agglomerates up to 5.5 μm are observed.

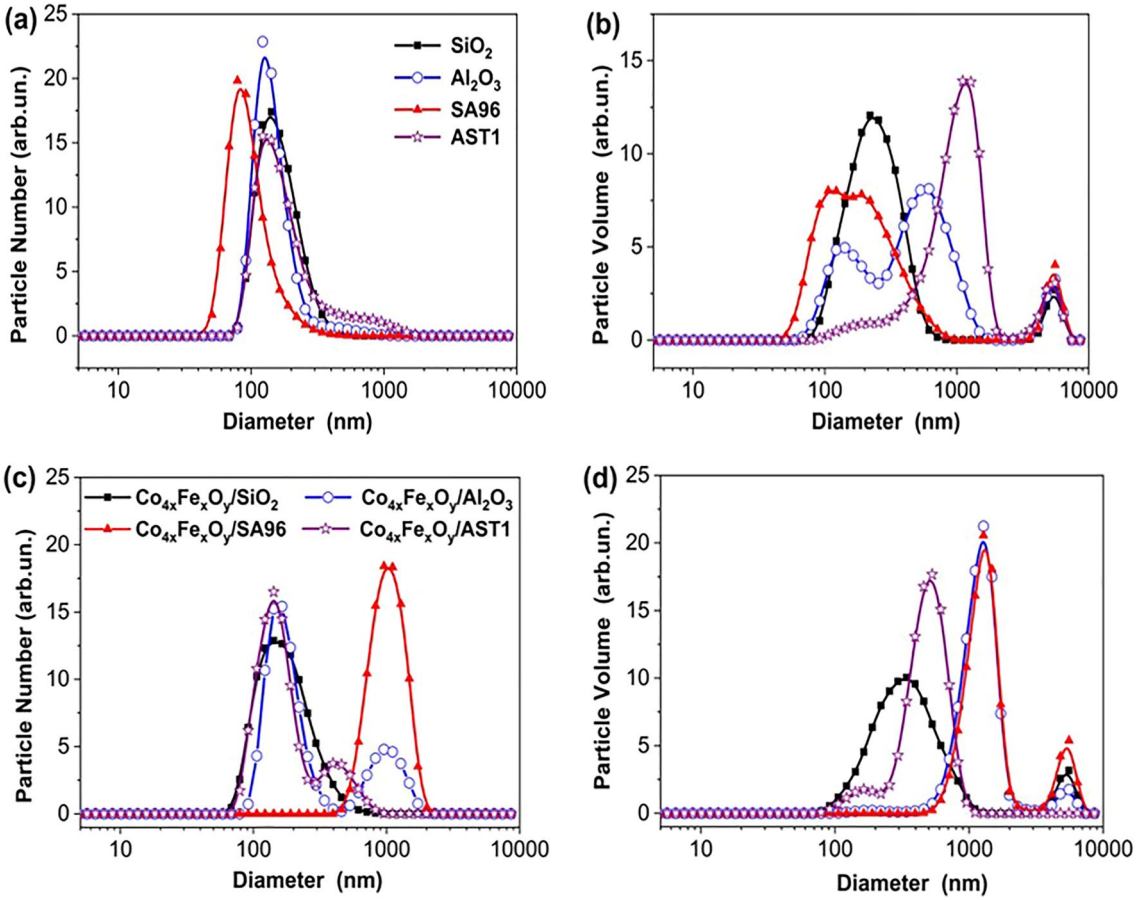

Fig. 10 PaSD related to the number **a**, **c** and the volume **b**, **d** for the initial fumed nanocarriers and NCs with $Co_{4x}Fe_xO_y$ after sonication (6 min) of the aqueous dispersions (C = 0.1 wt%)

Table 8 Characterization of $Co_{4x}Fe_xO_y$/fumed oxide NCs: Magnetization (M_s) at 300 K and coercivity (H_c) at 300 K

Composite	M_s, emu/g	H_c, Oe
$Co_{4x}Fe_xO_y/SiO_2$	7.75	386.5
$Co_{4x}Fe_xO_y/Al_2O_3$	5.8	56.5
$Co_{4x}Fe_xO_y$/SA96	4.42	43.05
$Co_{4x}Fe_xO_y$/AST1	3.68	117.8

There is a general tendency to increase the sizes of aggregates due to the modification of nanocarriers with the deposited $Co_{4x}Fe_xO_y$. This paper demonstrated the effects of various highly dispersed matrices on the magnetic properties of composites. Magnetic properties of the samples $Co_{4x}Fe_xO_y/SiO_2$, $Co_{4x}Fe_xO_y/Al_2O_3$, $Co_{4x}Fe_xO_y$/SA96 and $Co_{4x}Fe_xO_y$/AST1 are influenced by the fraction of pores and their distribution in the composites. Increasing the magnetic phase in the nanocomposites can provide promising adsorbents for the future application.

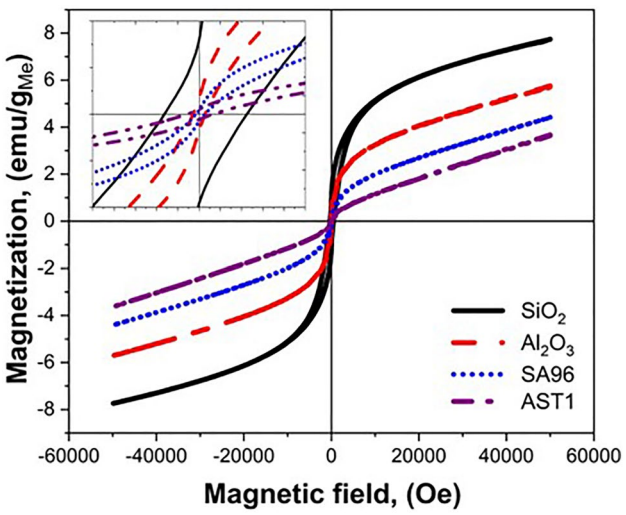

Fig. 11 Magnetic hysteresis loops of the $Co_{4x}Fe_xO_y$/fumed oxide NCs: $Co_{4x}Fe_xO_y$/Si60, $Co_{4x}Fe_xO_y/A_2O_3$, $Co_{4x}Fe_xO_y$/SA96 and $Co_{4x}Fe_xO_y$/AST1 at room temperature. Insert zoom-in of the coercive behaviour

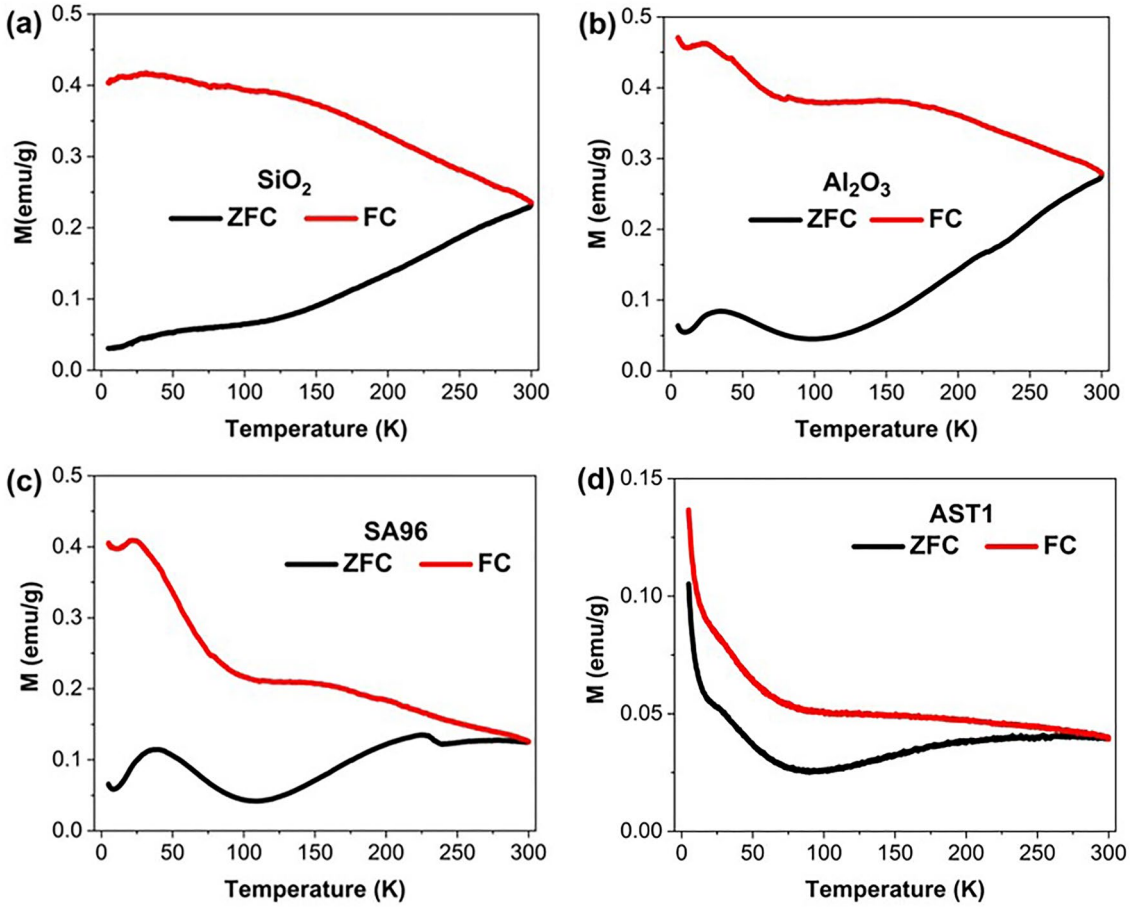

Fig. 12 ZFC and field-cool (FC) cooling magnetization for the $Co_{4x}Fe_xO_y$/fumed oxide NCs, measured with H = 100 Oe: (a) $Co_{4x}Fe_xO_y/SiO_2$, (b) $Co_{4x}Fe_xO_y/Al_2O_3$, (C) $Co_{4x}Fe_xO_y$/SA96 and (d) $Co_{4x}Fe_xO_y$/AST1

Acknowledgements The authors are grateful for the financial support of the International Visegrad Fund (Dr. Iryna Sulym, Contract number 52210724; D.Sc. Olena Goncharuk, Contract number 52211441) as well as to Professor V.M. Gun'ko for the developing and providing the program for the pore size distribution calculation.

Author contributions AD—Conceptualization, Investigation, Writing—original draft. OI—Data curation. IS—SEM, ASAP, Writing—original draft. SD—SEM, ASAP. EP—synthesis, FTIR. MB—XRD. LS—investigation of magnetical properties. LA—particle size distribution. OG—Conceptualization, Investigation, Writing—original draft. KT—Writing—original draft.

Funding Alla Dyachenko, Olena Ischenko, Sternik Dariusz, Eugen Pakhlov, Mykola Borysenko, Lyudmila Storozhuk, Lyudmila Andriyko—No funding. Iryna Sulym—International Visegrad Fund, 52210724. Olena Goncharuk—International Visegrad Fund, 52211441. Konrad Terpilowski—International Visegrad Fund, 52211441 and 52210724.

Data availability The data will be available at the e-mail address terpil@umcs.pl.

Declarations

Competing interests The authors declare no competing interests.

Ethical approval Not applicable.

References

1. Havancsák, K.: Nanotechnology at present and its promise for the future. Mater. Sci. Forum **414**, 85–94 (2003). https://doi.org/10.4028/www.scientific.net/MSF.414-415.85
2. Mohseni, E., Mendizadeh, M.B., Jian, Y., Ali, Y.M.: Single and combined effects of nano-SiO_2, nano-Al_2O_3 and nano-TiO_2 on the mechanical, rheological and durability properties of

self-compacting mortar containing fly ash. Constr. Build. Mater. **84**, 331–340 (2015). https://doi.org/10.1016/j.conbuildmat.2015.03.006
3 Tamirat, Y.: The role of nanotechnology in semiconductor industry: review article. J. Mater. Sci. Nanotechnol. **5**, 202–229 (2017). https://doi.org/10.15744/2348-9812.5.202
4. Gun'ko, V.M., Leboda, R., Skubiszewska-Zięba, J.: Heating effects on morphological and textural characteristics of individual and composite nanooxides. Adsorption **15**, 89–98 (2009). https://doi.org/10.1007/s10450-009-9160-2
5. Chibowski, S., Wiśniewska, M., Wawrzkiewicz, M., Hubicki, Z., Goncharuk, O.: Electrokinetic properties of silica-titania mixed oxide particles dispersed in aqueous solution of C.I. Direct Yellow 142 dye—effects of surfactant and electrolyte presence. Physicochem. Probl. Miner. Process. **56**, 6–13 (2020). https://doi.org/10.37190/ppmp/123612
6. Chowdhury, A.-N., Rahim, A., Ferdosi, Y.J., Azam, M.S., Hossain, M.M.: Cobalt–nickel mixed oxide surface: a promising adsorbent for the removal of PR dye from water. Appl. Surf. Sci. **256**, 3718–3724 (2010). https://doi.org/10.1016/j.apsusc.2010.01.013
7. Wawrzkiewicz, M., Wiśniewska, M., Gun'ko, V.M., Zarko, V.I.: Adsorptive removal of acid, reactive and direct dyes from aqueous solutions and wastewater using mixed silica–alumina oxide. Powder Technol. **278**, 306–315 (2015). https://doi.org/10.1016/j.powtec.2015.03.035
8. Wiśniewska, M., Wrzesińska, K., Wawrzkiewicz, M., Chibowski, S., Urban, T., Goncharuk, O., Gun'ko, V.M.: Alumina-silica-titania adsorbent for hazardous azo and phthalocyanine dyes removal from textile baths and wastewaters—the impact of ionic surfactants. Physicochem. Prob. Miner. Process. **56**, 178–193 (2020). https://doi.org/10.37190/ppmp/128214
9. Borai, E.H., El-Dessouky, S.I., Hassan, H.S.: Mixed silica and alumina hosted carboxylate oxide for removal of chromium species from wastewater. Adsorption **13**, 61–71 (2007). https://doi.org/10.1007/s10450-007-9001-0
10. Ciesielczyk, F., Bartczak, P., Wieszczycka, K., Siwińska-Stefańska, K., Nowacka, M., Jesionowski, T.: Adsorption of Ni(II) from model solutions using co-precipitated inorganic oxides. Adsorption **19**, 423–434 (2013). https://doi.org/10.1007/s10450-012-9464-5
11. Heredia, A., Gómez Avila, J., Vinuesa, A., Saux, C., Mendoza, S.M., Garay, F., Crivello, M.: Compared arsenic removal from aqueous solutions by synthetic mixed oxides and modified natural zeolites. Adsorption **25**, 1425–1436 (2019). https://doi.org/10.1007/s10450-019-00109-2
12. Ismail, A.A., El-Midany, A.A., Ibrahim, I.A., Matsunaga, H.: Heavy metal removal using SiO_2–TiO_2 binary oxide: experimental design approach. Adsorption **14**, 21–29 (2008). https://doi.org/10.1007/s10450-007-9042-4
13. Rudziński, W., Charmas, R.: Effects of surface heterogeneity of oxides in simple ion adsorption at oxide/electrolyte interfaces. Adsorption **2**, 245–255 (1996). https://doi.org/10.1007/BF00128306
14. Wiśniewska, M., Bogatyrov, V., Ostolska, I., Szewczuk-Karpisz, K., Terpiłowski, K., Nosal-Wiercińska, A.: Impact of poly(vinyl alcohol) adsorption on the surface characteristics of mixed oxide Mn_xO_y–SiO_2. Adsorption **22**, 417–423 (2016). https://doi.org/10.1007/s10450-015-9696-2
15. Wiśniewska, M., Nowicki, P., Bogatyrov, V.M., Nosal-Wiercińska, A., Pietrzak, R.: Comparison of adsorption properties of Mg_xO_y–SiO_2 and Zn_xO_y–SiO_2 in the mixed oxide-poly(vinyl alcohol) system. Colloids Surf A Physicochem Eng Asp **492**, 12–18 (2016). https://doi.org/10.1016/j.colsurfa.2015.12.013
16. Wiśniewska, M., Wawrzkiewicz, M., Wołowicz, A., Goncharuk, O.: Nanosized oxides of different compositions as adsorbents for hazardous substances removal from aqueous solutions and wastewaters. In: Fesenko, O., Yatsenko, L. (eds.) Nanooptics, nanophotonics, nanostructures, and their applications, pp. 103–126. Springer, Cham (2018)
17 Wiśniewska, M., Urban, T., Grządka, E., Zarko, V.I., Gun'ko, V.M.: Comparison of adsorption affinity of polyacrylic acid for surfaces of mixed silica–alumina. Colloid Polym. Sci. **292**, 699–705 (2014). https://doi.org/10.1007/s00396-013-3103-x
18. Wiśniewska, M., Ostolska, I., Szewczuk-Karpisz, K., Chibowski, S., Terpiłowski, K., Gun'ko, V.M., Zarko, V.I.: Investigation of the polyvinyl alcohol stabilization mechanism and adsorption properties on the surface of ternary mixed nanooxide AST 50 (Al_2O_3–SiO_2–TiO_2). J. Nanopart. Res. **17**, 12–26 (2015). https://doi.org/10.1007/s11051-014-2831-2
19. Behrens, S., Appel, I.: Magnetic nanocomposites. Curr. Opin. Biotechnol. **39**, 89–96 (2016). https://doi.org/10.1016/j.copbio.2016.02.005
20. Mourdikoudis, S., Kostopoulou, A., LaGrow, A.P.: Magnetic nanoparticle composites: synergistic effects and applications. Adv. Sci. **8**, 2004951 (2021). https://doi.org/10.1002/advs.202004951
21. Giraldo, L., Erto, A., Moreno-Piraján, J.C.: Magnetite nanoparticles for removal of heavy metals from aqueous solutions: synthesis and characterization. Adsorption **19**, 465–474 (2013). https://doi.org/10.1007/s10450-012-9468-1
22. Fadillah, G., Yudha, S.P., Sagadevan, S., Fatimah, I., Muraza, O.: Magnetic iron oxide/clay nanocomposites for adsorption and catalytic oxidation in water treatment applications. Open Chem. **18**, 1148–1166 (2020). https://doi.org/10.1515/chem-2020-0159
23. Ramirez, S., Chan, K., Hernandez, R., Recinos, E., Hernandez, E., Salgado, R., Khitun, A.G., Garay, J.E., Balandin, A.A.: Thermal and magnetic properties of nanostructured ferrimagnetic composites with graphene–graphite fillers. Mater. Des. **118**, 75–80 (2016). https://doi.org/10.1016/j.matdes.2017.01.018
24 Ali, A., Zafar, H., Zia, M., Ihsan Ul, H., Rehman, P.A., Ali, J.S., Hussain, A.: Synthesis, characterization, applications, and challenges of iron oxide nanoparticles. Nanotechnol. Sci. Appl. **9**, 49–67 (2016). https://doi.org/10.2147/NSA.S99986
25. Duvenhage, D.J., Coville, N.J.: Fe:Co/TiO_2 bimetallic catalysts for the Fischer–Tropsch reaction: part 3: the effect of Fe: Co ratio, mixing and loading on FT product selectivity. Appl. Catal. A Gen. **289**, 231–239 (2005). https://doi.org/10.1016/j.apcata.2005.05.008
26. Matzui, LYu., Vovchenko, L.L., Syvolozhskyi, O.A., Yakovenko, O.S., Borovoy, M.O., Gomon, O.O., Dyachenko, A.G., Ischenko, O.V., Vakaliuk, A.V., Bodnaruk, A.V., Kalita, V.M.: Structure and magnetic properties of MWCNTs decorated by NiFe, CoFe, NiCo nanoparticles. Mol. Cryst. Liq. Cryst. **752**, 77–94 (2023). https://doi.org/10.1080/15421406.2022.2091275
27 O'Shea, V.A., Álvarez-Galván, M.C., Campos-Martin, J.M., Menéndez, N.N., Tornero, J.D., Fierro, J.L.G.: Surface and structural features of Co–Fe oxide nanoparticles deposited on a silica substrate. Eur. J. Inorg. Chem. **24**, 5057–5068 (2006). https://doi.org/10.1002/ejic.200600778
28. Yathindranath, V., Worden, M., Sun, Z., Miller, D.W., Hegmann, T.: A general synthesis of metal (Mn, Fe Co, Ni, Cu, Zn) oxide and silica nanoparticles based on a low temperature reduction/hydrolysis pathway. RSC Adv. **3**, 23722–23729 (2013). https://doi.org/10.1039/c3ra44565h
29 Zhludenko, M., Dyachenko, A., Bieda, O., Gaidai, S., Filonenko, M., Ischenko, O.: Structure and catalytic properties of Co–Fe systems in the reaction of CO_2 methanation. Acta Phys. Polonica A **133**, 1084–1087 (2018). https://doi.org/10.12693/APhysPolA.133.1084
30. Huang, X., Chen, Z.: Sol–gel preparation and characterization of $CoFe_2O_4$–SiO_2 nanocomposites. Solid State Commun. **132**, 845–850 (2004). https://doi.org/10.1016/j.ssc.2004.09.060

31. Teoh, L.G., Li, K.-D.: Synthesis and characterization of NiO nanoparticles by sol–gel method. Mater. Trans. **53**, 2135–2140 (2012). https://doi.org/10.2320/matertrans.M2012244
32. Dalai, A.K., Bakhshi, N.N., Esmail, M.N.: Characterization studies of plasma-sprayed cobalt and iron catalysts. Ind. Eng. Chem. Res. **31**, 1449–1457 (1992). https://doi.org/10.1021/ie00006a005
33. Borysenko, M.V., Gun'ko, V.M., Dyachenko, A.G., Sulim, I.Y., Leboda, R., Skubiszewska-Zieba, J., Ryczkowski, J.: CVD-zirconia on fumed silica and silica gel. Appl. Surf. Sci. **242**, 1–12 (2005). https://doi.org/10.1016/j.apsusc.2004.07.064
34. Dry, M.E.: The Fischer–Tropsch synthesis. In: Anderson, J.R., Boudart, M. (eds.) Catalyst science technology, pp. 159–255. Springer-Verlag, Berlin (1981)
35. Beach, E.R., Shqau, K., Brown, S.E., Rozeveld, S.J., Morris, P.A.: Solvothermal synthesis of crystalline nickel oxide nanoparticles. Mater. Chem. Phys. **115**, 371–377 (2009). https://doi.org/10.1016/j.matchemphys.2008.12.018
36. Kievit, F.M., Stephen, Z.R., Veiseh, O., Arami, H., Wang, T.Z., Lai, V.P., Park, J.O., Ellenbogen, R.G., Disis, M.L., Zhang, M.Q.: Targeting of primary breast cancers and metastases in a transgenic mouse model using rationally designed multifunctional SPIONs. ACS Nano **6**, 2591–2601 (2012). https://doi.org/10.1021/nn205070h
37. Laurent, S., Forge, D., Port, M., Roch, A., Robic, C., Elst, L.V., Muller, R.N.: Magnetic iron oxide nanoparticles: synthesis, stabilization, vectorization, physicochemical characterizations, and biological applications. Chem. Rev. **108**, 2064–2110 (2008). https://doi.org/10.1021/cr068445e
38. Li, P., Nan, C.Y., Wei, Z., Lu, J., Peng, Q., Li, Y.: Mn_3O_4 nanocrystals: facile synthesis, controlled assembly, and application. Chem. Mater. **22**, 4232–4236 (2010). https://doi.org/10.1021/cm100831q
39. Dyachenko, A.G., Ischenko, O.V., Borysenko, M.V., Gaidai, S.V., Yatsymyrskyi, A.V., Tsapyuk, G.G., Pryhunova, O.V., Kostyrko, O.O.: Co–Fe/Al_2O_3 nanocomposite catalysts of the process of CO_2 hydrogenation. Theoret. Exp. Chem. **58**, 134–142 (2022). https://doi.org/10.1007/s11237-022-09731-8
40. Bi, Y., Dalai, A.K.: Selective production of C_4 hydrocarbons from syngas using Fe–Co/ZrO_2 and SO_4^{2-}/ZrO_2 catalysts. Can. J. Chem. Eng. **81**, 230–242 (2003). https://doi.org/10.1002/cjce.5450810208
41. Kandhasamy, N., Ramalingam, G., Murugadoss, G., Kumar, R.M., Manibalan, G., JothiRamalingam, R., Yadav, H.M.: Copper and zinc oxide anchored silica microsphere: a superior pseudocapacitive positive electrode for aqueous supercapacitor applications. J. Alloys Compd. **888**, 161489 (2021). https://doi.org/10.1016/j.jallcom.2021.161489
42. Sulym, I., Wiśniewska, M., Storozhuk, L., Terpilowski, K., Sternik, D., Borysenko, M., Derylo-Marczewska, A.: Investigation of surface structure, electrokinetic and stability properties of highly dispersed Ho_2O_3–Yb_2O_3/SiO_2 nanocomposites. Appl. Nanosci. **12**, 553–554 (2022). https://doi.org/10.1007/s13204-021-01710-0
43 Sulym, I., Goncharuk, O., Skwarek, E., Sternik, D., Borysenko, M.V., Derylo-Marczewska, A., Wladyslaw, J., Gun'ko, V.M.: Silica-supported ceria–zirconia and titania–zirconia nanocomposites: structural characteristics and electrosurface properties. Colloids Surf A Physicochem Eng Asp **482**, 631–638 (2015). https://doi.org/10.1016/j.colsurfa.2015.07.015
44. Corrias, A., Casula, M., Ennas, G., Marras, S., Navarra, G., Mountjoy, G.J.: X-ray absorption spectroscopy study of FeCo–SiO_2 nanocomposites prepared by the sol–gel method. Phys. Chem. B **107**, 3030–3039 (2003). https://doi.org/10.1021/jp027078h
45 Dyachenko, A., Ischenko, O., Goncharuk, O., Borysenko, M., Mischanchuk, O., Gun'ko, V., Sternik, D., Lisnyak, V.: Preparation and characterization of Ni–Co/SiO_2 nanocomposite catalysts for CO_2 methanation. Appl. Nanosci. **12**, 349–358 (2022). https://doi.org/10.1007/s13204-020-01650-1
46. Mallampati, R., Valiyaveettil, S.: Biomimetic metal oxides for the extraction of nanoparticles from water. Nanoscale **5**, 3395–3399 (2013). https://doi.org/10.1039/C3NR34221B
47 Gaidai, S.V., Gryn'ko, V.S., Zhludenko, M.G., Dyachenko, A.G., Tkach, V.M., Ishchenko, O.V.: Activity of carbon-fiber-supported Fe–Co catalysts in the CO_2 methanation reaction. J. Superhard Mater. **39**, 122–128 (2017). https://doi.org/10.3103/S1063457617020071
48. Gregg, S.J., Sing, K.S.W.: Adsorption, surface area and porosity. Academic Press, London (1982)
49 Gun'ko, V.M.: Composite materials: textural characteristics. Appl. Surf. Sci. **307**, 444–454 (2014). https://doi.org/10.1016/j.apsusc.2014.04.055
50. JCPDS Database, International Center for Diffraction Data, PA 2001 Available: http://www.icdd.com
51. Monshi, A., Foroughi, M., Monshi, R.: Modified Sherrer equation to estimate more accurately nano-cristallite size using XRD. World J. Nano Sci. Eng. **2**, 154–160 (2012). https://doi.org/10.4236/wjnse.2012.23020
52. Thommes, M., Kaneko, K., Neimark, A.V., Olivier, J.P., Rodriguez-Reinoso, F., Rouquerol, J., Sing, K.S.W.: Physisorption of gases, with special reference to the evaluation of surface area and pore size distribution (IUPAC technical report). Pure Appl. Chem. (2015). https://doi.org/10.1515/pac-2014-1117
53. Gun'ko, V.M., Turov, V.V., Zarko, V.I., Goncharuk, O.V., Pakhlov, E.M., Skubiszewska-Zięba, J., Blitz, J.P.: Interfacial phenomena at a surface of individual and complex fumed nanooxides. Adv. Colloid Interface Sci. **235**, 108–189 (2016). https://doi.org/10.1016/j.cis.2016.06.003
54. Senthil, V.P., Gajendiran, J., Raj, S.G., Shanmugavel, T., Ramesh, K.G., Parthasaradhi, R.C.: Study of structural and magnetic properties of cobalt ferrite ($CoFe_2O_4$) nanostructures. Chem. Phys. Lett. **695**, 19–23 (2018). https://doi.org/10.1016/j.cplett.2018.01.057
55. Tang, Ch.W., Wang, Ch.B., Chien, Sh.H.: Characterization of cobalt oxides studied by FT-IR, Raman, TPR and TG-MS. Thermochim. Acta **473**, 68–73 (2008). https://doi.org/10.1016/j.tca.2008.04.015
56. Kurtan, U., Topkaya, R., Baykal, A., Toprak, M.S.: Temperature dependent magnetic properties of $CoFe_2O_4$/CTAB nanocomposite synthesized by sol–gel auto-combustion technique. Ceram. Int. **39**, 6551 (2013). https://doi.org/10.1016/j.ceramint.2013.01.088
57. Waldron, R.D.: Infrared spectra of ferrites. Phys. Rev. **99**, 1727–1735 (1955). https://doi.org/10.1103/PhysRev.99.1727
58 Biesinger, M.C., Payne, B.P., Grosvenor, A.P., Lau, L.W.M., Gerson, A.R., Smart, R.S.C.: Resolving surface chemical states in XPS analysis of first row transition metals, oxides and hydroxides: Cr, Mn, Fe, Co and Ni. Appl. Surf. Sci. **257**, 2717–2730 (2011). https://doi.org/10.1016/j.apsusc.2010.10.051
59. Ischenko, O.V., Dyachenko, A.G., Saldan, I., Lisnyak, V.V., Diyuk, V.E., Vakaliuk, A.V., Yatsymyrskyi, A.V., Gaidai, S.V., Zakharova, T.M., Makota, O., Ericsson, T., Häggström, L.: Methanation of CO_2 on bulk Co–Fe catalysts. Int. J. Hydrogen Energy **46**, 37860–37871 (2021). https://doi.org/10.1016/j.ijhydene.2021.09.034
60. Mullet, M., Khare, V., Ruby, C.: XPS study of Fe(II)–Fe(III) (oxy) hydroxycarbonate green rust compounds. Surf. Interface Anal. **40**, 323–328 (2008). https://doi.org/10.1002/sia.2758
61. McCafferty, E., Wightman, J.P.: Determination of the concentration of surface hydroxyl groups on metal oxide films by a quantitative XPS method. Surf. Interface Anal. **26**, 549–564 (1998)
62. Rui, M., Peng, Yu.: The influences of matrix materials on the magnetic and mechanical properties of $Fe_{78}Si_9B_{13}$ soft magnetic composites fabricated by injection molding. Mater. Res. Bull. **139**, 111256 (2021). https://doi.org/10.1016/j.materresbull.2021.111256

63. Wang, L., Qiao, J., Zheng, W., Cai, Y., Ying, W., Li, S., Che, JYu.: Microstructure and properties of FeSiCr/PA6 composites by injection molding using FeSiCr powders by phosphating and coupling treatment. J. Magn. Magn. Mater. **452**, 210–218 (2018). https://doi.org/10.1016/j.jmmm.2017.12.067